PAPER

Graphene-based stretchable and transparent moisture barrier

Graphene-based stretchable and transparent moisture barrier

Sejeong Won[1] ⬤, **Do Van Lam**[1,2], **Jin Young Lee**[3], **Hyun-June Jung**[4], **Min Hur**[3] ⬤, **Kwang-Seop Kim**[1,2], **Hak-Joo Lee**[4] **and Jae-Hyun Kim**[1,2] ⬤

[1] Nano-Convergence Mechanical Systems Research Division, Korea Institute of Machinery & Materials (KIMM), Daejeon 34103, Republic of Korea
[2] Korea University of Science and Technology (UST), 217 Gajeong-ro, Yuseong-gu, Daejeon 34113, Republic of Korea
[3] Plasma Engineering Laboratory, Korea Institute of Machinery & Materials (KIMM), Daejeon 34103, Republic of Korea
[4] Center for Advanced Meta-Materials (CAMM), Daejeon 34103, Republic of Korea

E-mail: jaehkim@kimm.re.kr

Abstract
We propose an alumina-deposited double-layer graphene (2LG) as a transparent, scalable, and stretchable barrier against moisture; this barrier is indispensable for foldable or stretchable organic displays and electronics. Both the barrier property and stretchability were significantly enhanced through the introduction of 2LG between alumina and a polymeric substrate. 2LG with negligible polymeric residues was coated on the polymeric substrate via a scalable dry transfer method in a roll-to-roll manner; an alumina layer was deposited on the graphene via atomic layer deposition. The effect of the graphene layer on crack generation in the alumina layer was systematically studied under external strain using an *in situ* micro-tensile tester, and correlations between the deformation-induced defects and water vapor transmission rate were quantitatively analyzed. The enhanced stretchability of alumina-deposited 2LG originated from the interlayer sliding between the graphene layers, which resulted in the crack density of the alumina layer being reduced under external strain.

Supplementary material for this article is available online

Keywords: double-layer graphene, barrier, aluminium oxide, roll-to-roll transfer, stretchable display

(Some figures may appear in colour only in the online journal)

1. Introduction

Stretchable displays based on organic light-emitting diodes (OLEDs) have attracted considerable attention by offering user-friendly design and multifunctional features such as foldable screens and electronic skins [1, 2]. Organic materials are considered promising candidates for thin and lightweight displays with stretchability [1–4]. Because these materials are extremely vulnerable to moisture and oxygen, a barrier layer is essential. It is also necessary for this layer to be stretchable, transparent, and scalable.

Thin film encapsulation has frequently been adopted for generating flexible transparent barriers. Barrier materials with much lower permeabilities have been developed by reducing defect density. Inorganic materials are regularly used for barrier layers, and extensive research related to fabrication process parameters, including various chemistries, deposition methods, and thicknesses, has been performed to reduce defect densities [5–11]. Among these materials, the bilayer coating of Al_2O_3/parylene C exhibits superior barrier properties [10] and a defect free, ultrathin layer of thermally grown SiO_2 was employed as a water barrier for active, flexible electronic systems [11]. While the inorganic materials have a low water vapor transmission rate (WVTR) compared to polymeric materials, they are easily fractured under mechanical deformations, and their barrier properties degrade

owing to the formation of cracks. An inorganic indium zinc oxide (IZO)/SiO$_x$/Al$_2$O$_3$ multilayer exhibited barrier performance up to a bending radius of 35 mm (the corresponding tensile strain is ~0.27%) [12]. An inorganic/organic hybrid structure is known to be better than a single inorganic layer regarding barrier performance under mechanical deformation [13]. However, the commercial application of such barriers to flexible displays has been limited because of the complicated manufacturing process and low resistance to strain [12, 14].

Graphene has become a popular option for use as a flexible transparent film because of its high specific surface area, flexibility, and optical transparency [15–21]. Defect-free monolayer graphene is known to be impermeable to all gases and liquids, and the hydrophobic surface of graphene prevents the permeation of water vapor [18, 22, 23]. As a result, graphene and its derivatives, including graphene/polymer nanocomposites, graphene oxide, and graphene nanosheets, have been investigated for use as flexible transparent barrier films [16, 24–26]. Among these, chemical vapor-deposited (CVD) graphene is considered to be the most prospective barrier film because it does not require an additional process for homogeneous mixing in polymer matrices and additionally, it can also be formed as a multilayered structure with scalability [27]. Furthermore, several works on CVD graphene have demonstrated the possibility of using it as a graphene-based barrier [15, 28–30]. Until now, the properties of CVD graphene barriers are still inferior to those of inorganic materials, and their polymethyl methacrylate(PMMA)-based transfer method suffers from poor scalability and polymeric residue.

In this study, we propose a stretchable and transparent moisture barrier for stretchable or foldable display applications. This barrier was developed by inserting a dry-transferred double-layer graphene (2LG) between an inorganic layer and a polyimide film, which are common materials for foldable OLED displays. The polyimide film is commonly used as a substrate of display panels due to its high heat resistance. The 2LG was fabricated using a roll-to-roll dry-transfer technology to demonstrate its scalability. The behaviors of crack generation and evolution in alumina layers with and without 2LG were characterized using *in situ* tensile tests. The crack densities on the alumina layers were drastically reduced through the insertion of 2LG. The effect of the 2LG on the WVTR of the barrier was quantitatively characterized with respect to the applied strain.

2. Experimental details

2.1. Growth and transfer of graphene onto the polyimide substrate

Monolayer graphene was synthesized on a Cu foil by a CVD process. A 35 μm thick Cu foil was used as a catalysis for graphene synthesis, and was preheated at 400 °C for 30 min with 300 sccm of Ar and 10 sccm of H$_2$ at 640 mTorr. A precursor gas of methane (CH$_4$) was introduced with a flow rate of 15 sccm at 1000 °C for 30 min after annealing of the Cu foil at 1000 °C for 30 min. The CVD chamber was then cooled to room temperature with 300 sccm of Ar and 10 sccm of H$_2$ for 2 h.

Following the growth of graphene, 2LG was fabricated on a target substrate by dry transfer using a dispersive adhesion medium and a hot roller. A polyethylene terephthalate (PET) with a silicone adhesive layer was used as the dispersive adhesion medium to support the single-layer graphene during etching of the copper foil. The PET/silicone film was attached to the graphene-grown Cu foil using the roll-to-roll transfer machine under a nip force per unit width of 22.05 N mm^{-1} and a roller speed of 500 mm min^{-1}. The Cu foil was etched by a 0.1 M ammonium persulfate ((NH$_4$)$_2$S$_2$O$_8$, Sigma-Aldrich) solution containing 5 mM imidazole (C$_3$H$_4$N$_2$, Sigma-Aldrich) and 50 mM sulfuric acid (H$_2$SO$_4$, Sigam-Alrdich). The PET/silicone/graphene was rinsed with deionized water for 30 min and dried. The PET/silicone/graphene and the 25 μm thick polyimide substrate were inserted between heated rollers (95 °C) under a nip force per unit width of 2.45 N mm^{-1} and a roller speed of 250 mm min^{-1}, to enable the transfer of single-layer graphene on the polyimide substrate. The above roll-to-roll transfer process was repeated to fabricate 2LG.

### 2.2. Deposition of Al$_2$O$_3$ on 2LG/polyimide

The polyimide substrate and 2LG/polyimide structure were loaded into a thermal ALD chamber (S200, Savannah). The chamber was then evacuated to ~0.1 Torr under a 20 sccm N$_2$ flow. The deposition was carried out at 70 °C using trimethylaluminum (Al(CH$_3$)$_3$, TMA, Aldrich) and H$_2$O as precursors. ALD was set in the exposure mode to ensure uniform deposition of Al$_2$O$_3$. For each ALD cycle, the H$_2$O pulse was 0.1 s in duration, followed by a 20 s exposure, and 30 s purging time; followed by, 0.015 s in duration, 20 s exposure, and 30 s purging time for the TMA pulse. We also included Si pieces as reference samples to estimate the growth rate of Al$_2$O$_3$.

2.3. Tensile test with in situ optical microscopy measurements

The barrier samples were cut into rectangular strips of 3 mm widths and gage lengths of 15 mm for tensile tests. *In situ* optical microscopic observations were carried out during the uniaxial tensile tests to study generation and propagation of crack and buckling delamination of the Al$_2$O$_3$ layers. This enabled the quantitative measurement of the cracks and buckling delaminations at a variety of applied strain without release of the strain. Densities of crack and buckling delamination were defined as the total length of cracks and buckling delamination per unit area [31, 32]. The adopted microscopic system had a working distance of 19 mm and 20X magnification.

2.4. WVTR measurement before and after the tensile test

WVTR was measured using the water vapor transmission testing system (Permatran_W3/33, Mocon, Inc.). The samples were measured at 37.8 °C at 90% RH with 1 cm^2 active
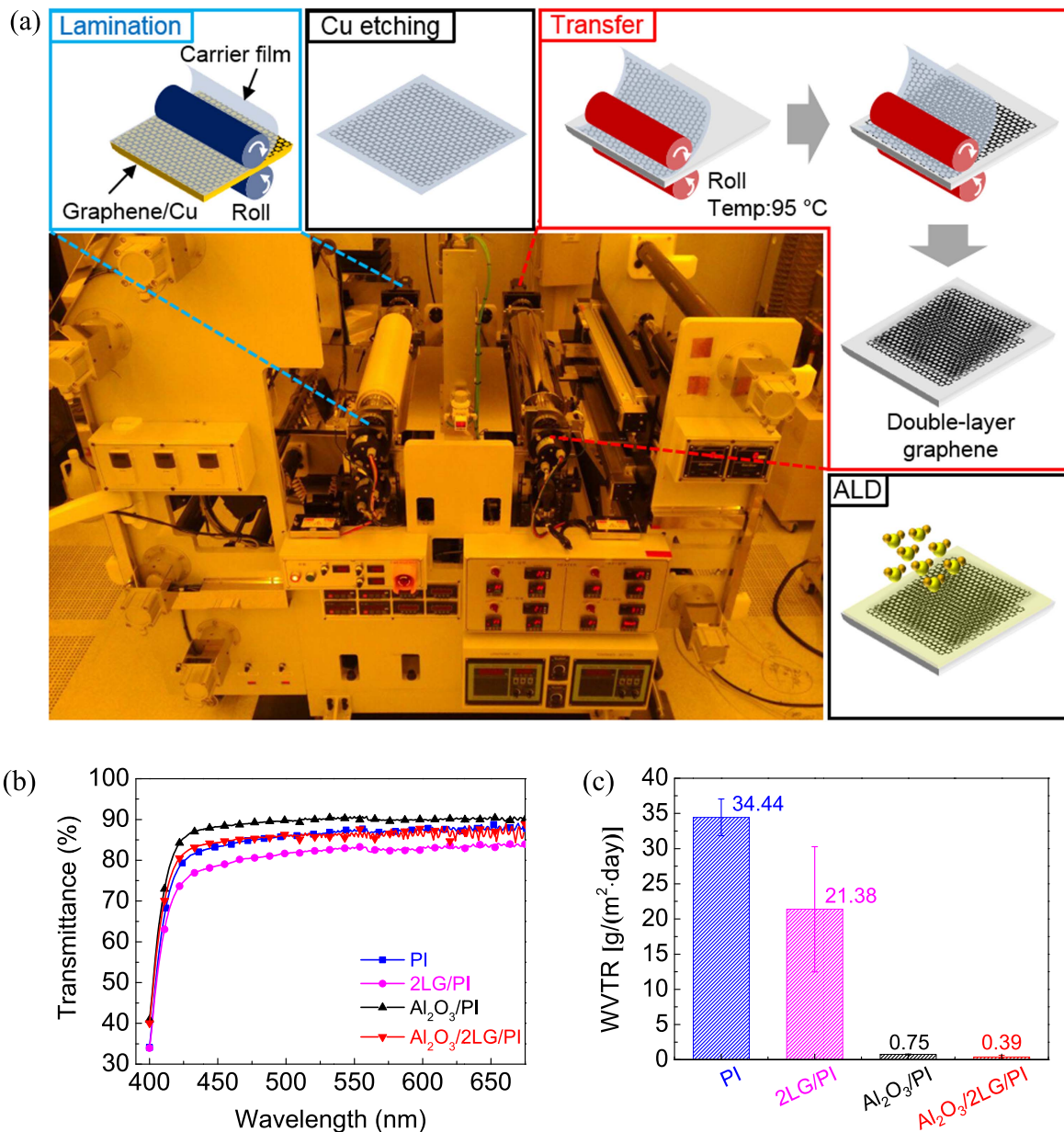
Figure 1. (a) Schematics showing sample preparation procedure with a photograph of roll-to-roll transfer machine used for graphene transfer. (b) Transmittances of PI, Al_2O_3/PI, 2LG/PI, and Al_2O_3/2LG/PI. (c) WVTR values of PI, Al_2O_3/PI, 2LG/PI and Al_2O_3/2LG/PI at 38 °C and 90% relative humidity.

sample area. The nitrogen flow rate was set as 10 sccm. WVTR values were measured after the WVTR change has been stabilized and saturated. The number of measurement cycles was set as more than 30 according to the recommended procedure of Mocon Incorporation.

3. Results and discussion

3.1. Preparation and characterization of barrier films

Figure 1(a) shows a schematic diagram of the sample preparation procedure and a photograph of the roll-to-roll transfer machine. To obtain the 2LG, a single-layer CVD graphene was transferred twice onto a PI substrate using the roll-to-roll

transfer machine. The custom-made roll-to-roll transfer machine is equipped with a force and temperature control to reduce mechanical damage during the transfer of graphene as described in [33]. Stacked 2LG with negligible polymer residue on a flexible substrate using dispersive adhesion and a hot roller is demonstrated during this preparation phase. For obtaining the Al_2O_3/2LG barrier, the Al_2O_3 layer was deposited using atomic layer deposition (ALD) at 70 °C on the transferred 2LG. The Al_2O_3 nucleated around the wrinkles and point defects of the CVD graphene at the initial stage of deposition; the nuclei grew larger and coalesced with the adjacent nuclei to form a continuous film with the increase of the ALD cycle [34, 35]. Regarding the fabrication of the Al_2O_3 barrier, an Al_2O_3 layer was directly deposited on the PI substrate using ALD to produce a conformal inorganic

coating [7]. The thickness of the Al_2O_3 layer was measured to be 47 nm by using the ellipsometry measurement method.

Atomic force microscopy (AFM) was used to identify the surface morphology of the barriers (figure S1 is available online at stacks.iop.org/NANO/29/125705/mmedia). The surface of an untreated PI substrate shows a root mean square roughness of 0.28 ± 0.08 nm. When the Al_2O_3 layer was deposited directly onto the PI surface, a granular-like surface was formed (surface roughness: 0.54 ± 0.08 nm). Because the transferred CVD graphene was generally accompanied with wrinkles and defects [34], the roughness increased further to 0.95 ± 0.34 nm through the transfer of a 2LG onto the PI. The AFM image of Al_2O_3/2LG/PI shows that the alumina layer is deposited along the morphology of the transferred graphene (surface roughness: 1.21 ± 0.56 nm).

The transmittances of the barriers are shown in figure 1(b). Given that a value of 550 nm is a peak wavelength of visible light, the transmittance of visible light was measured at this wavelength. The transmittance of PI and Al_2O_3/PI are 87.6 and 90.7%, respectively; the transmittance increased after the deposition of the Al_2O_3 layer. Because the Al_2O_3 layer is characterized by a lower refractive index than the PI substrate, it functioned as an antireflection coating [36]. The 2LG/PI and Al_2O_3/2LG/PI films showed corresponding transmittances of 82.9 and 85.8%, respectively. The results indicate that the transmittance of 2LG decreases only by $\sim$4.7%, which is in good agreement with previous results [37, 38].

Water is thousand times more detrimental for OLEDs compared to oxygen at room temperature [14]; therefore, a low WVTR is necessary for reliable organic electronics. In the case of multilayer graphene, polymer residue between the graphene layers increases the WVTR values by functioning as spacers between the graphene layers, which would accelerate water diffusion [15, 30]. Therefore, PET/silicone was adopted to transfer single-layer graphene. Because the PET/silicone film uses dispersive adhesion, polymer residue does not remain on the transferred graphene, unlike thermal release tape (TRT) with foaming agents which results in a lot of polymeric residues. AFM investigation was performed to verify the polymer residue on the transferred graphene. Residues on graphene could be scratched using an AFM tip during contact mode scanning because the residues have low mechanical and adhesion strengths with graphene. Contact mode scanning was performed to scratch residues on the graphene on a $1 \mu m \times 1 \mu m$ area with a contact force of 10 nN. Subsequently, the surface topography of the area, including the scratched area, was obtained using the non-contact mode (figure S2). In the case of graphene transferred by PET/silicone, there is no difference in the height between the scratched and the non-scratched areas. However, graphene transferred using TRT shows a height difference of 1.51 nm. Thus, there is negligible polymer residue on graphene transferred using PET/silicone in contrast to that transferred via TRT.

WVTR values of the different barriers are shown in figure 1(c). When the WVTR value of the bare PI film was 34.44 ($\pm$2.6) g m^{-2} d^{-1}, the WVTR values of 2LG/PI, Al_2O_3/PI, and Al_2O_3/2LG/PI were 21.38 ($\pm$8.9), 7.50×10^{-1} ($\pm 5.0 \times 10^{-2}$), and 3.85×10^{-1} ($\pm 2.3 \times 10^{-1}$) g m^{-2} d^{-1}, respectively. The results show that the barrier property was considerably improved by the deposition of the Al_2O_3 layer, and that the 2LG also functioned as a barrier layer.

To evaluate the barrier property of 2LG, Al_2O_3 and Al_2O_3/2LG, the barrier improvement factor (BIF), which expresses the barrier performance of the laminated structure, was estimated. The BIF is defined as the ratio between the WVTR value of the unlaminated barrier film to that of the laminate structure [39]. BIFs of the 2LG, Al_2O_3, and Al_2O_3/2LG were 1.61, 45.92, and 89.45, respectively (figure S3(a)). The BIF of Al_2O_3/2LG was 1.9 times larger than that of Al_2O_3. The BIFs of 2LG and Al_2O_3/2LG were compared with those of other graphene barriers [15, 28, 29] according to the number of graphene layers (figure S3(b)). The BIF of 2LG was similar to that of the 2LG transferred using the conventional PMMA transfer method [15, 28]. The BIF of Al_2O_3/2LG was noticeably larger than that of any graphene-based barrier, including 6-layer graphene reported in other works reviewed in this study.

3.2. Tensile tests with in situ optical microscopic observations

Because stretchable barriers are often exposed to mechanical deformations during their manufacturing and operation periods, it is crucial to consider deformation-induced defects on the barrier films, such as cracks, delamination, and wrinkles. A composite layer of Al_2O_3 and single-layer graphene has been proposed as a flexible barrier up to a bending strain of approximately 0.89% [40]. For the development of a stretchable barrier, deformation-induced defects on the barrier should be kept low under a wider range of mechanical strains.

The oxide barrier coating on polymer substrates represents brittle films on deformable substrates. Cracking of a brittle film on a ductile substrate has been primarily studied using the shear lag analysis [41, 42]. This shear lag model describes the stress transfer between two layers via an interfacial shear stress. When a tensile strain is applied to a substrate with a thin film on it, interfacial shear stress occurs between the thin film and the substrate, and as such, the thin film experiences tensile strain due to the shear stress. When the tensile stress exceeds the tensile strength of the thin film, a crack occurs. In our previous research, we confirmed that the crack density of indium tin oxide (ITO) decreased via the reduction of interfacial shear stress owing to interlayer sliding of multilayer graphene. Furthermore, we described the sliding behavior of the multilayer graphene using the shear lag model [43].

Despite the decrease of the interfacial shear stress as the number of graphene layer increases, there are disadvantages such as the reduction of transmittance and increase in cost. In addition, from experimental results, the effect of a tri-layer graphene on the crack density of a barrier material was similar to that of a 2LG. Figures S4(a) and (b) show the crack densities and WVTR values for Al_2O_3/1LG/PI, Al_2O_3/2LG/PI and Al_2O_3/3LG/PI as a function of strain, respectively. The difference in the crack
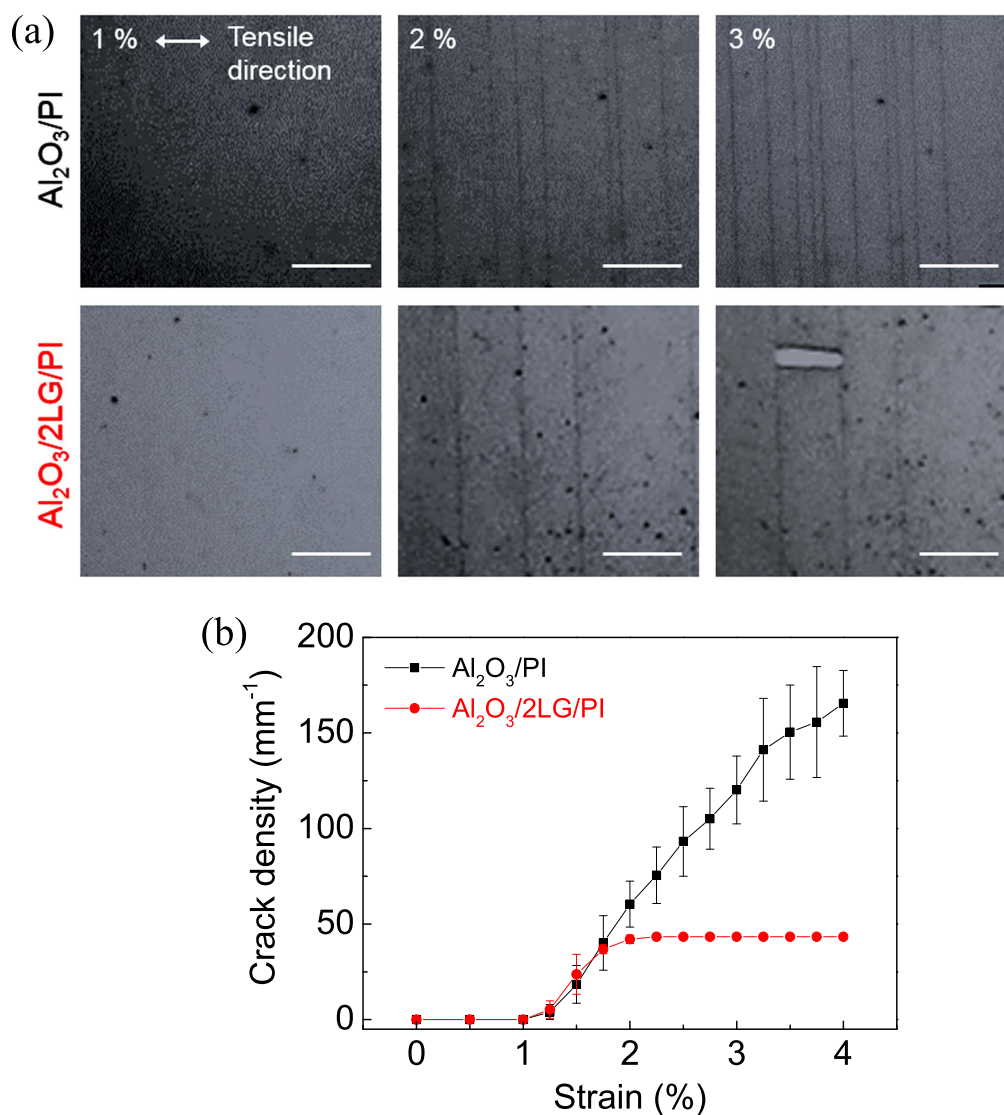
Figure 2. (a) Optical microscopy images of the Al_2O_3/PI and Al_2O_3/2LG/PI layers under tensile strains of 1%, 2% and 3%. Scale bar is 20 μm. (b) Cracks densities of Al_2O_3/PI and Al_2O_3/2LG/PI, with respect to the applied tensile strain.

density of Al_2O_3/3LG/PI and Al_2O_3/2LG/PI caused by tensile deformation was not significant. However, the crack density of Al_2O_3/1LG/PI was much higher than that of Al_2O_3/2LG/PI because Al_2O_3/1LG/PI has no interlayer sliding of graphene layers. With regards to crack density, the WVTR of Al_2O_3/2LG/PI was lower than that of Al_2O_3/1LG/PI, and it was the same or slightly higher than that of Al_2O_3/3LG/PI. Therefore, a 2LG that is the smallest layer of a multilayer graphene was utilized as a strain relaxer between the barrier material and the polymeric substrate.

Tensile tests of Al_2O_3/PI with and without 2LG were carried out to quantitatively investigate cracks under the controlled mechanical strain. Figure 2(a) shows the optical microscopy images of the two types of barriers with 1%, 2%, and 3% strains. In both cases, cracks appeared in the form of straight lines perpendicular to the direction of the tensile load. At the initial stage of loading, some cracks were generated with a wide inter-spacing distance. When the applied strain

was increased, more cracks were generated between the existing cracks and the width of the generated cracks widened. The crack density of Al_2O_3/2LG/PI was lower than that of Al_2O_3/PI under the same strain. In the case of Al_2O_3/2LG/PI, buckling delamination activated by transverse compression induced by Poisson's effect was observed. Figure S5 shows the AFM image of Al_2O_3/2LG/PI after tensile deformation, which exhibits the buckling delamination of the barriers.

The densities of the crack were measured as a function of the applied strain by analyzing the optical microscopy images obtained *in situ* during the tests [31, 32]. As shown in figure 2(b), the crack density of Al_2O_3/PI increases rapidly with an increase of the strain. However, the crack density of Al_2O_3/2LG/PI is significantly lower than that of the Al_2O_3/PI for a given strain, and the crack density of Al_2O_3/2LG/PI saturates above a strain of 2%, accompanied by an increase of the crack width.

The lower crack density of $Al_2O_3/2LG/PI$ implies a decreased transfer of strain from the PI substrate to the Al_2O_3 layer. The reason for this decreased strain transfer in the multilayer structure is the interlayer sliding of the structure. This sliding mostly occurs at the interfaces characterized by the lowest adhesion between the adjacent layers. Figure S6(a) shows a schematic representation of the detachment of the Al_2O_3 from $Al_2O_3/2LG/PI$ after the tensile test. To compare the interlayer adhesion in the $Al_2O_3/2LG/PI$, a surface analysis was performed on the delaminated Al_2O_3 and the residual surface. Figure S6(b) shows the Raman spectra of bare tape and the delaminated Al_2O_3. The G and 2D peaks from the Raman shift plot indicate the presence of graphene on the delaminated Al_2O_3, thus confirming that the delaminated Al_2O_3 consists of Al_2O_3 and graphene. For the residual surface, AFM analysis was performed because Raman spectral analysis was not efficient due to the background signal of the PI substrate. Figures S6(c) and (d) show the topographies and normalized frictional forces, respectively, of the residual surface and the bare PI substrate. The residual surface contains considerable wrinkles and has a lower frictional force than that of the bare PI substrate. As the frictional force of the PI substrate decreases after the transfer of graphene onto its surface, the low friction implies that graphene remained on the PI substrate. From these analyses, it is concluded that the adhesion between the upper and lower graphene was weaker than that of the other two interfaces and the decrease of strain transfer is mainly due to the sliding of the graphene interlayers. Interlayer sliding occurs easily in artificially stacked multilayer graphene, owing to weak adhesion between the graphene layers [43, 44].

3.3. WVTR measurements after tensile deformation

The WVTR of a barrier film can be much higher than the intrinsic WVTR of the barrier material when the barrier film has pinholes and macroscopic defects because such defects act as accelerated gas diffusion paths [5, 9, 45]. It was observed that few large defects contributed most of the permeation [46]. To investigate the effect of 2LG on barrier property under tensile deformation, WVTR measurements were performed on Al_2O_3/PI and $Al_2O_3/2LG/PI$ after the tensile tests, up to a tensile strain of 3%. The strain range was selected because the plastic deformation of polyimide films began to occur between a strain of 2% and 3% [47, 48]. The samples used were 20 mm wide rectangular strips with a gage length of 90 mm to allow both tensile tests and WVTR measurements. Figure 3(a) shows the WVTR and the crack density of Al_2O_3/PI and $Al_2O_3/2LG/PI$ after tensile deformation. Each data was obtained by repeating the test at least three times. Overall, the WVTR increases with increasing strain in both barriers. The WVTR of $Al_2O_3/2LG/PI$ is much lower than that of Al_2O_3/PI, by a factor of three, after deformation of the same strain. In accordance with the results of the WVTR measurements, the crack density of $Al_2O_3/2LG/PI$ is also much lower than that of Al_2O_3/PI

under the same strains. In the case of Al_2O_3/PI, the WVTR and crack density increases rapidly with the applied strain. However, in the case of $Al_2O_3/2LG/PI$, the WVTR increases with increasing crack density up to a strain of 2%, and after that, the WVTR continues to increase despite barely any noticeable incremental change in the crack density.

In addition, to confirm the effect of 2LG under repeated loadings, the crack densities and WVTR values after performing the cyclic tests were measured. The cyclic tests were conducted under strain control at a frequency of 1 Hz. A mean strain of 2.5% and a strain amplitude of 0.5% were chosen by considering the elastic region of the PI substrate. The WVTR values and the crack densities were normalized by dividing the WVTR value and the crack density of $Al_2O_3/2LG/PI$ after 1 cycle to confirm a stability under cyclic loading. Figure S7 shows the normalized WVTR values and crack densities of $Al_2O_3/2LG/PI$ with respect to the number of loading cycles. The normalized values of $Al_2O_3/2LG/PI$ remained close to 1 up to 10 000 cycles, demonstrating a high cyclic stability.

Figure 3(b) shows the relationship between the WVTR and crack density. The range of tensile strain is from 0% to 3%. Because permeation is dependent linearly on the defect radius (or the perimeter) instead of the area of defect, the WVTR of the whole barrier is linearly proportional to the multiplication of the mean radius and defect density [49]. Crack, is a type of defect, also deteriorates barrier characteristics, and the WVTR is strongly associated with crack density [50]. Therefore, the relation between the WVTR and crack density was assumed to be linear. In the case of $Al_2O_3/2LG/PI$, along with the impact of crack density, the effects of buckling delamination and graphene barrier were combined. Therefore, the sections before and after the buckling delamination occurred were divided and the relationships between the WVTR and crack density were obtained. In general, the WVTR of the Al_2O_3/PI increased rapidly with high crack densities, while that of $Al_2O_3/2LG/PI$ was low with low crack densities. In the case of Al_2O_3/PI, the WVTR increased with a slope of 0.13 as the strain increased. However, for $Al_2O_3/2LG/PI$, the slope was as low as 0.02 and increased after the buckling delamination occurred.

Before the buckling delamination, the WVTR of $Al_2O_3/2LG/PI$ increased with a much lower slope than that of Al_2O_3/PI. Moreover, $Al_2O_3/2LG/PI$ still had a lower WVTR after the buckling delamination occurred. To investigate the reason for this, the $Al_2O_3/2LG/PI$ films were observed using SEM after the tensile test. The SEM images shown in figure 3(c) reveal that the graphene layer is exposed both in the cracked and buckling delamination areas. This implies that the graphene layer that was exposed after the crack and buckling delamination of the Al_2O_3 layer still acted as a barrier layer.

Figure 4 shows the schematics of the two barrier structures under tensile deformation. In the case of Al_2O_3/PI, the crack density in the Al_2O_3 layer grows fast with the increasing tensile strain, and as a result, the WVTR increases
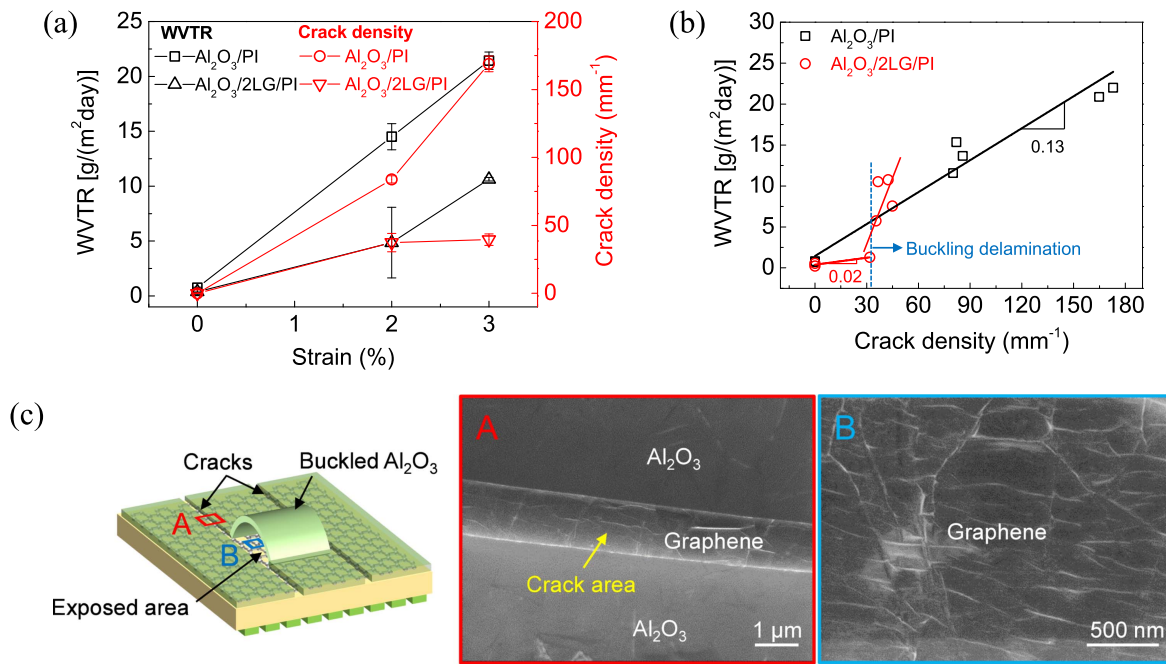
Figure 3. (a) WVTR values and crack densities of Al_2O_3/PI and Al_2O_3/2LG/PI after tensile deformation. (b) WVTR values according to the crack densities of Al_2O_3/PI and Al_2O_3/2LG/PI. The range of the tensile strain is from 0% to 3%. (c) Schematic and SEM images of the Al_2O_3/2LG/PI after the tensile test. A is the cracked area and B is the exposed area after buckling delamination. SEM images of A and B show that graphene layer is exposed both in the cracked and buckling delamination areas.
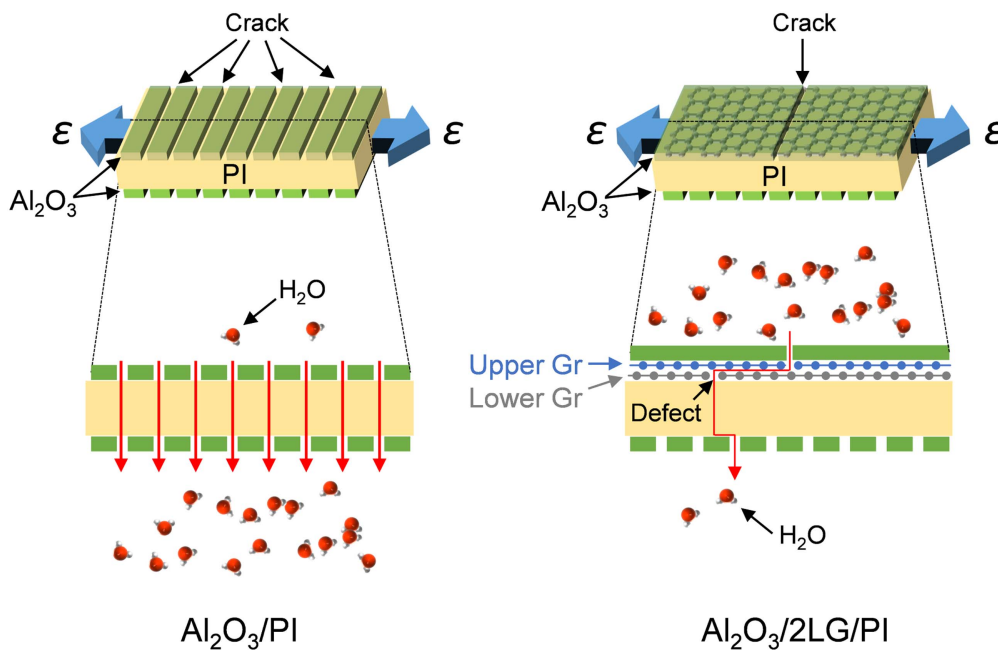
Figure 4. Schematic representation of the proposed mechanism for water vapor diffusion through Al_2O_3/PI and Al_2O_3/2LG/PI after tensile deformation.

rapidly. This is because the bare PI substrate is exposed where the cracks of the Al_2O_3 layer are generated. In the case of Al_2O_3/2LG/PI, the crack density becomes much lower than that of Al_2O_3/PI owing to the decreased strain transfer due to the sliding of the graphene layers. Moreover, the graphene layer that remains on the crack and buckling delamination areas act as the barrier layer for water vapors.

4. Conclusions

A transparent and stretchable moisture barrier was developed by inserting dry transferred 2LG between an Al_2O_3 layer and a polyimide film. The Al_2O_3/2LG/PI film showed a much lower crack density than that of its Al_2O_3/PI counterpart under tensile deformation. The WVTR of the Al_2O_3/2LG/PI

film was measured to be three times lower than that of Al_2O_3/PI after a tensile deformation of 2%. It was found that strain transfer between Al_2O_3 and PI was greatly reduced through the insertion of 2LG, and that graphene under the alumina functioned as a hydrophobic barrier for moisture diffusion. This study has therefore confirmed that the dry transferred 2LG can be used for enhancing the stretchability of inorganic barriers, which is a scalable and promising solution for stretchable and transparent moisture barrier for stretchable and foldable OLED displays.

Acknowledgments

ORCID iDs

Sejeong Won ⓘ https://orcid.org/0000-0003-4400-5121
Min Hur ⓘ https://orcid.org/0000-0002-6355-2182
Jae-Hyun Kim ⓘ https://orcid.org/0000-0002-4327-2992

References

[1] Wang C, Hwang D, Yu Z, Takei K, Park J, Chen T, Ma B and Javey A 2013 User-interactive electronic skin for instantaneous pressure visualization *Nat. Mater.* **12** 899–904

[2] Sekitani T, Nakajima H, Maeda H, Fukushima T, Aida T, Hata K and Someya T 2009 Stretchable active-matrix organic light-emitting diode display using printable elastic conductors *Nat. Mater.* **8** 494–9

[3] Liang J, Li L, Niu X, Yu Z and Pei Q 2013 Elastomeric polymer light-emitting devices and displays *Nat. Photonics* **7** 817–24

[4] Sun N, Wang Q, Zhao Y, Chen Y, Yang D, Zhao F, Chen J and Ma D 2014 High-performance hybrid white organic light-emitting devices without interlayer between fluorescent and phosphorescent emissive regions *Adv. Mater.* **26** 1617–21

[5] Klumbies H *et al* 2015 Thickness dependent barrier performance of permeation barriers made from atomic layer deposited alumina for organic devices *Org. Electron.* **17** 138–43

[6] Hirvikorpi T *et al* 2014 Barrier properties of plastic films coated with an Al_2O_3 layer by roll-to-roll atomic layer deposition *Thin Solid Films* **550** 154–69

[7] Ahmadzada T, Mckenzie D R, James N L, Yin Y and Li Q 2015 Atomic layer deposition of Al_2O_3 and Al_2O_3/TiO_2 barrier coatings to reduce the water vapour permeability of polyetheretherketone *Thin Solid Films* **591** 131–6

[8] Henry B M, Erlat A G, McGuigan A, Grovenor C R M, Briggs G A D, Tsukahara Y, Miyamoto T, Noguchi N and Niijima T 2001 Characterization of transparent aluminum oxide and indium tin oxide layers on polymer substrates *Thin Solid Films* **382** 194–201

[9] Barker C P, Kochem K H, Revell K M, Kelly R S A and Badyal J P S 1995 Atomic force microscopy and permeability study of stretching-induced gas barrier loss of AlO_x layers *Thin Solid Films* **259** 46–52

[10] Caldwell R, Mandal H, Sharma R, Solzbacher F, Tathireddy P and Rieth L 2017 Analysis of Al_2O_3-parylene C bilayer coatings and impact of microelectrode topography on long term stability of implantable neural arrays *J. Neural Eng.* **14** 046011

[11] Fang H *et al* 2016 Ultrathin, transferred layers of thermally grown silicon dioxide as biofluid barriers for biointegrated flexible electronic systems *Proc. Natl Acad. Soc.* **18** 11682–7

[12] Lee G H, Yun J, Lee S, Jeong Y, Jung J H and Cho S H 2010 Investigation of brittle failure in transparent conductive oxide and permeation barrier oxide multilayers on flexible polymers *Thin Solid Films* **518** 3075–80

[13] Vähä-Nissi M, Sunberg P, Kauppi E, Hirvikorpi T, Sievänen J, Sood A, Karppien M and Harlin A 2012 Barrier properties of Al_2O_3 and alucone coatings and nanolaminates on flexible biopolymer films *Thin Solid Films* **520** 6780–5

[14] Yu D, Yang Y Q, Chen Z, Tao Y and Liu Y F 2016 Recent progress on thin-film encapsulation technologies for organic electronic devices *Opt. Commun.* **362** 43–9

[15] Choi K *et al* 2015 Reduced water vapor transmission rate of graphene gas barrier films for flexible organic field-effect transistors *ACS Nano* **9** 5818–24

[16] Su Y, Kravets V G, Wong S L, Waters J, Geim A K and Nair R R 2014 Impermeable barrier films and protective coatings based on reduced graphene oxide *Nat. Commun.* **5** 4843–7

[17] Zhao Y, Xie Y, Hui Y Y, Tang L, Jie W, Jiang Y, Xu L, Lau S P and Chai Y 2013 Highly impermeable and transparent graphene as an ultra-thin protection barrier for Ag thin films *J. Mater. Chem.* C **1** 4956–61

[18] Li N, Huang X, Zhang H, Li Y and Wang C 2017 Transparent and self-supporting graphene films with wrinkled-graphene-wall-assembled opening polyhedron building blocks for high performance flexible/transparent supercapacitors *ACS Appl. Mater. Interfaces* **9** 9763–71

[19] Li N, Yang G, Sun Y, Song H, Cui H, Yang G and Wang C 2015 Free-standing and transparent graphene membrane of polyhedron box-shaped basic building units directly grown using a NaCl template for flexible transparent and stretchable solid-state supercapacitors *Nano Lett.* **5** 3195–203

[20] Li N, Huang X, Zhang H, Shi Z, Li Y and Wang C 2017 NaCl multistage recrystallization-induced formation of 3D micro-structured ribbon-like graphene based films for high performance flexible/transparent supercapacitors *J. Mater. Chem.* A **5** 14595–603

[21] Li N, Hyang X, Zhang H, Shi Z and Wang C 2017 Graphene-hollow-cubes with network-faces assembled a 3D micro-strucured transparent and free-standing film for high performance supercapacitors *J. Mater. Chem.* A **5** 16803–11

[22] Bunch J S, Verbridge S S, Alden J S, van der Zande A M, Parpia J M, Craighead H G and McEuen P L 2008 Impermeable atomic membranes from graphene sheets *Nano Lett.* **8** 2458–62

[23] Kim T, Kang J H, Yang S J, Sung S J, Kim Y S and Park C R 2014 Facile preparation of reduced graphene oxide–based gas barrier films for organic photovoltaic devices *Energy Environ. Sci.* **7** 3403–11

[24] Yamaguchi H *et al* 2014 Reduced graphene oxide thin films as ultrabarriers for organic electronics *Adv. Energy Mater.* **4** 1300986

[25] Tseng I H, Liao Y F, Chiang J C and Tsai M H 2012 Transparent polyimide/graphene oxide nanocomposite with improved moisture barrier property *Mater. Chem. Phys.* **136** 247–53

[26] Lee S, Hong J Y and Jang J 2013 Multifunctional graphene sheets embedded in silicone encapsulant for superior performance of light-emitting diodes *ACS Nano* **7** 5784–90

[27] Pierleoni D, Xia Z Y, Christian M, Ligi S, Minelli M, Morandi V, Doghieri F and Palermo V 2016 Graphene-based coatings on polymer films for gas barrier applications *Carbon* **96** 503–12

[28] Seo H K, Park M H, Kim Y H, Kwon S J, Jeong S H and Lee T W 2016 Laminated graphene films for flexible transparent thin film encapsulation *ACS Appl. Mater. Interfaces* **8** 14725–31

[29] Seo T H *et al* 2016 Tailored CVD graphene coating as a transparent and flexible gas barrier *Sci. Rep.* **6** 24143

[30] Wirtz C, Berner N C and Duesberg G S 2015 Large-scale diffusion barriers from CVD grown graphene *Adv. Mater. Interfaces* **2** 1500082

[31] Zhu X F, Zhang B, Gao J and Zhang G P 2009 Evaluation of the crack-initiation strain of a Cu-Ni multilayer on a flexible substrate *Scr. Mater.* **60** 178–81

[32] Niu R M, Liu G, Wang C, Zhang G, Ding X D and Sun J 2007 Thickness dependent critical strain in submicron Cu films adherent to polymer substrate *Appl. Phys. Lett.* **90** 161907

[33] Jang B, Kim C H, Choi S T, Kim K S, Kim K S, Lee H J, Cho S, Ahn J H and Kim J H 2017 Damage mitigation in roll-to-roll transfer of CVD-graphene to flexible substrates *2D Mater.* **4** 024002

[34] Shin W C, Bong J H, Choi S Y and Cho B J 2013 Functionalized graphene as an ultrathin seed layer for the atomic layer deposition of conformal high-K dielectrics on graphene *App. Mater. Interfaces* **5** 11515–9

[35] Lam D V, Kim S M, Cho Y, Kim J H, Lee H J, Yang J M and Lee S M 2014 Healing defective CVD-graphene through vapor phase treatment *Nanoscale* **6** 5639–44

[36] Hedayati M K and Elbahri M 2016 Antireflective coatings: Conventional stacking layers and ultrathin plasmonic metasurfaces, a mini-review *Materials* **9** 497

[37] Nair R R, Blake P, Grigorenko A N, Novoselov K S, Booth T J, Stauber T, Peres N M R and Geim A K 2008 Fine structure constant defines visual transparency of graphene *Science* **320** 1308

[38] Hwangbo Y, Lee C K, Mag-Isa A E, Jang J W, Lee H J, Lee S B, Kim S S and Kim J H 2014 Interlayer non-coupled optical properties for determining the number of layers in arbitrarily stacked multilayer graphenes *Carbon* **77** 454–61

[39] Greener J, Ng K C, Vaeth K M and Smith T M 2007 Moisture permeability through multilayered barrier films as applied to flexible OLED display *J. Appl. Polym. Sci.* **106** 3534–42

[40] Nam T, Park Y J, Lee H, Oh I K, Ahn J H, Cho S M, Kim H and Lee H B R 2017 A composite layer of atomic-layer-deposited Al_2O_3 and graphene for flexible moisture barrier *Carbon* **116** 553–61

[41] McGuigan A P, Briggs G A D, Burlakov V M, Yanaka M and Tsukahara Y 2003 An elastic-plastic shear lag model for fracture of layered coatings *Thin Solid Films* **424** 219–23

[42] Sun J, Lu N, Yoon J, Oh K, Suo Z and Vlassak J J 2009 Inorganic islands on a highly stretchable polyimide substrate *J. Mater. Res.* **24** 3338–42

[43] Won S *et al* 2016 A graphene metainterface for enhancing the stretchability of brittle oxide layers *Nanoscale* **8** 4961–8

[44] Won S *et al* 2014 Double-layer CVD graphene as stretchable transparent electrodes *Nanoscale* **6** 6057–64

[45] da Silva Sobrinho A S, Czeremuszkin G, Latrèche M and Wertheimer M R 2000 Defect-permeation correlation for ultrathin transparent barrier coatings on polymers *J. Vac. Sci. Technol.* A **18** 149–57

[46] Blunt L, Elrawemi M, Fleming L and Sweeney F 2013 Correlation of micro and nano-scale defects with WVTR for aluminium oxide barrier coatings for flexible photovoltaic modules *Int. J. Precis. Technol.* **3** 290–302

[47] Chen M, Yin J, Jin R, Yao L, Su B and Lei Q 2015 Dielectric and mechanical properties and thermal stability of polyimide-graphene oxide composite films *Thin Solid Films* **584** 232–7

[48] Mohri M, Nili-Ahmadabadi M, PouryazdanPanah M and Hahn H 2016 Evaluation of structure and mechanical properties of Ni-rich NiTi/Kapton composite film *Mater. Sci. Eng.* A **668** 13–9

[49] Klumbies H, Karl M, Hermenau M, Rösch R, Seeland M, Hoppe H, Müller-Meskamp L and Leo K 2014 Water ingress into and climate dependent lifetime of organic photovoltaic cells investigated by calcium corrosion tests *Sol. Energy Mater. Sol. Cells* **120** 685–90

[50] Park E K, Kim S, Heo J and Kim H J 2016 Electrical evaluation of crack generation in SiN_x and SiO_xN_y thin-film encapsulation layers for OLED displays *Appl. Surf. Sci.* **370** 126–30